Article

Measurement of Near-Surface Current Shear Using a Lagrangian Platform and Its Implication on Microplastic Dispersion

Jun-Ho Lee [1] and Jun Myoung Choi [2],*

1   Research Vessel Nara, Pukyong National University, Busan 608-737, Republic of Korea
2   Department of Ocean Engineering, College of Environmental and Marine Sciences and Technology, Pukyong National University, Busan 608-737, Republic of Korea
*   Correspondence: jmchoi@pknu.ac.kr

Abstract: Air–sea interactions within the ocean's near-surface layer play a pivotal role in climate regulation and are essential for understanding the dispersion of marine pollutants such as microplastics and oil slicks. Despite its significance, high-resolution data exploring the physical dynamics near the air–sea interface are noticeably sparse. To address this, we introduced a novel Lagrangian observational platform, outfitted with an upward-facing high-resolution ADCP, designed to measure current shear within the top 2 m of the surface water. Through two short field experiments, we identified enhanced currents and shear in the near-surface layer, and observed a negative vertical momentum flux aligned with the wind direction and a positive one orthogonal to it. The measurement suggest that Stokes drift contributes to 10% of horizontal mass transport and 20% of shear in the top surface layer, with the direct and local wind-driven current being the predominant influence. To accurately model the physical behavior of buoyant microplastics, this observation underscores the necessity of parameterizations that account for both the Stokes drift and the direct, local wind-driven current, a factor that is often overlooked in many models.

Keywords: Lagrangian observational platform; surface current; ADCP; wind-driven current; Stokes drift; momentum flux; air–sea interaction

1. Introduction

Air–sea interactions in the near-surface layer are fundamental to our understanding of climatic systems and environmental phenomena. Within the surface boundary layer, these interactions comprise intricate processes at the interface, including the transfer of heat, momentum, and gases [1–3]. Physical processes near the air–sea interface, such as wind, wave, and current, regulate these transfers, serving as critical modulators of the exchange dynamics between the atmosphere and the ocean [4–8].

Specifically, currents within the top surface layer (TSL) at depths of 1–2 m are crucial for understanding air–sea interactions and for studying the behavior and dispersion of buoyant marine pollutants such as microplastics, copepod egg sacs, and oil spills [9]. The concentration of microplastics in the water increases exponentially towards the surface, indicating that microplastics predominantly reside and act within this layer, where wave-induced Stokes drift significantly enhances mass transport [10–12]. This effect is especially pronounced in coastal areas where wave deformations in shallow waters intensify nonlinearity, thereby influencing pollutant dispersion [13,14]. Many oceanic models struggle to directly represent the vertical shear within the TSL due to challenges in vertical resolution. As a result, this aspect is often parameterized and incorporated into models that focus on microplastic dispersion [12–15]. Observing near-surface currents is essential not only for quantifying pollutant horizontal dispersion but also for refining models that assess carbon exchange in relation to climate change [15–17].

Despite the significance of the upper ocean layer, our knowledge is limited due to the scarcity of high-resolution physical observations. The quest to understand or parameterize surface microplastics' behavior highlights the need for velocity measurements. Although many laboratory studies exist, precise field measurements of near-surface current shear are still lacking [18]. There is a distinct gap in observational data concerning surface current velocity, crucial for gauging the influence of Stokes drift on pollutants like microplastics. This shortfall is in part because of challenges in using Acoustic Doppler Current Profiler (ADCP) measurements to derive mean shear profiles within the TSL, stemming from the absence of appropriate observational platforms [19].

A variety of experimental methods, including current meters, moored ADCPs, X-band radars, polarimetric cameras, and drifters, have been employed to measure near-surface shear. Richman et al. [20] and Cronin and Kessler [21] took vertical shear measurements close to the surface, but the resolution of their current meter arrays decreased beneath depths of 2.5 m and 5 m, respectively. Wenegrat et al. [22] utilized low-frequency ADCP measurements at depths greater than 3.8 m to avoid issues related to surface boundary reflection [23]. Laxague et al. [19] succeeded in measuring shear over the top 1 cm layer using a polarimetric camera. They also collated and averaged previous ADCP and drifter data, highlighting the pronounced concentration of vertical shear within the TSL.

Lagrangian measurements are effective in tracking mean ocean currents and continuously evaluating local changes in surface currents. This approach aids in studying the immediate effects of wind-induced surface currents on a localized scale. Lagrangian drifters have been utilized to deduce surface currents [24,25], and Lagrangian observational platforms fitted with ADCPs have been employed to probe turbulence measurements [26,27]. A wave glider equipped with an ADCP has also demonstrated its proficiency as a platform for profiling near-surface currents. Most of these Lagrangian platforms are outfitted with down-looking ADCPs that commence measurements at a distance from the surface. Thomson [28] utilized a Lagrangian buoy with an up-looking ADCP to measure the rate of turbulence kinetic energy dissipation within the TSL. Despite significant advancements and novel approaches, direct and local measurements of near-surface mean current shear across diverse environments remain scarce and present considerable challenges.

In this study, we introduce a unique Lagrangian observational platform tailored to measure near-surface current shear and surface currents. These measurements are crucial for understanding the dynamics of buoyant pollutants and the nuances of air–sea interactions, areas that have been observed only to a limited degree in prior research. Equipped with a high-frequency 1 MHz ADCP, the platform excels in gauging current velocities within the top surface layer. We conducted two preliminary field experiments under diverse meteorological conditions. These experiments analyzed shifts in surface current speeds due to wind factors and scrutinized the influence of Stokes drift in relation to the total near-surface current in the TSL. Additionally, we estimated the role of Stokes drift in the shear dispersion [29,30] of microplastics within the TSL. Our results underscore that the Lagrangian observational platform adeptly pinpointed the intricate near-surface oceanic current shear, yielding profound insights into the dynamics of air–sea interactions and the influence of Stokes drift on microplastic dispersion in the uppermost layer.

2. Materials and Methods

2.1. Lagrangian Observational Platform

The Lagrangian measurement strategy is adept at mitigating potential issues arising from high-speed measurements in high-resolution ADCP data. In Eulerian stationary observations, the measured velocity includes the speed of the predominant mean flow. Notably, high velocities often result in a low Signal-to-Noise Ratio (SNR). As such, employing a Lagrangian platform, which inherently minimizes these significant velocities, enhances data quality. This approach also facilitates the continuous observation of the same water mass over a prolonged period by moving with the ambient water mass. In contrast, Eulerian platforms often struggle to monitor temporal variations of a specific water mass

because of the continuous movement of water masses at the observation location. Hence, our Lagrangian platform not only reduces potential disturbances from high-speed measurements but also consistently observes the same water mass along its path. However, for more extensive, longer-duration observations, especially when the primary objective is not surface current measurements, Eulerian platforms are preferable. They offer a lower risk of equipment loss and are better suited for long-term operation and upkeep.

We developed the Lagrangian Near-Surface Observational Platform (LANSOP) specifically to measure the mean current shear within the TSL (Figure 1). This platform consists of a 6 m long, slender metal structure that stands vertically within the surface layer, drifting passively with the ocean current. An up-looking ADCP, positioned approximately 2 m below the water surface, records the currents within the TSL. Due to issues with the weather station atop the structure, we sourced wind data from a nearby buoy and a terrestrial weather station for our analysis. The elongated structure was engineered to maintain its vertical orientation. Additionally, a wing placed opposite the ADCP was designed to pivot with the current, reducing potential data interference caused by the structure itself.
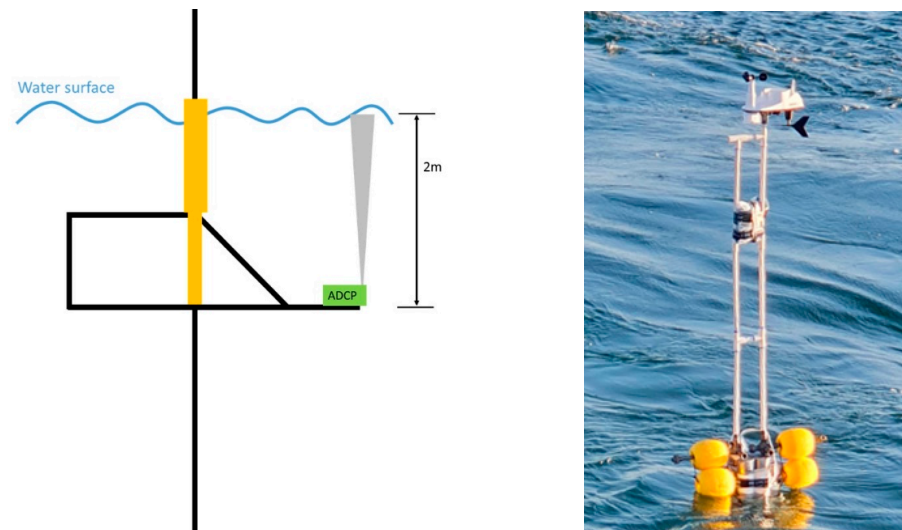

Figure 1. Schematic illustration of the Lagrangian Near-Surface Observational Platform (LANSOP) and a scene from the field experiment (Exp2) showcasing surface current measurement. The distance from the weather station at the top to the water surface is approximately 2 m. Owing to an issue with the attached weather station, we used wind data from nearby sources.

2.2. Field Experiments

The first experiment (Exp1) was executed on 6 May 2021, in the Korea Strait near Jeju Island, and the second experiment (Exp2) took place on 11 November 2021, in Yeongil Bay close to Pohang City (Figure 2). Both experiments were part of the R/V Nara Cruise, with mean water depths along the LANSOP trajectories being 68 m and 25 m for the respective experiments. LANSOP operated for 5 h during each experiment, from 11:30 AM to 4:30 PM KST in Exp1 and from 8 AM to 12:30 PM KST in Exp2. Over these periods, LANSOP drifted approximately 5.2 km and 2.2 km away from its initial locations for Exp1 and Exp2, respectively.
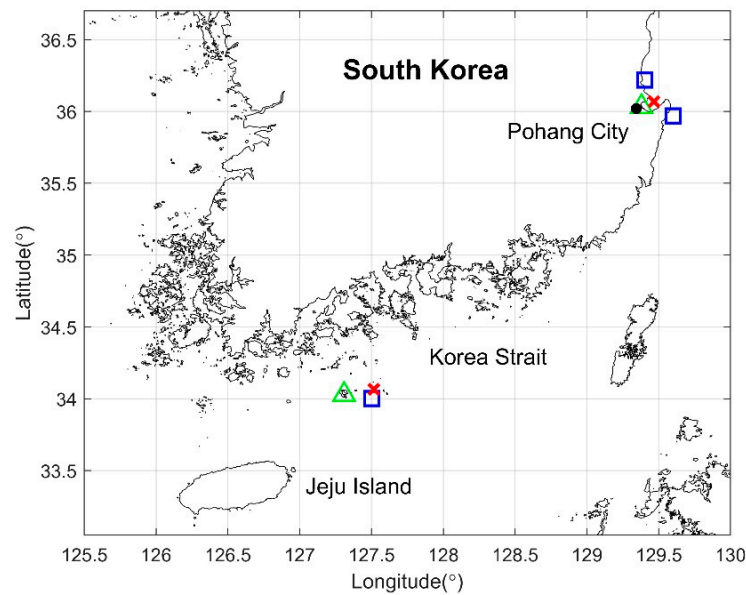
Figure 2. Locations of field experiments. The symbols 'x', '△', and '□' represent the mean location of LANSOP trajectory, the location of the wind station, and the locations of the wave buoys, respectively. Exp1 was conducted in the Korea Strait near Jeju Island on 6 May 2021, while Exp2 was conducted near Pohang City on 11 November 2021.

Hydrographical data for the experiments was sourced from the research vessel, adjacent buoys, and weather stations (Figure 2). For Exp1, conducted near Jeju Island, wind information was acquired both from the research vessel and a weather station situated on a nearby island (denoted by '△'). Wave data was collected from a proximate wave buoy (indicated by '□'). For Exp2, which took place near Pohang City, wind data was obtained from the research vessel and a weather station located in Pohang City. Wave information was retrieved from neighboring buoys.

2.3. Data Filtration

The SNR is a fundamental metric in ADCP data, defining the proportion between the desired signal's power and the background noise. A high SNR signifies superior signal strength compared to the noise, leading to more accurate and reliable measurements. Conversely, a low SNR can result in inferior signal quality, introducing errors and uncertainties into the data [31]. In order to remove the data with low SNR, we implemented a low SNR threshold at 3 dB. The side lobe effect refers to the undesirable emission or reception of acoustic energy deviating from the main beam direction. This phenomenon can introduce interference in upward-facing ADCP measurements when side lobes interact with the water's surface or other boundaries, thereby contaminating the desired signal [32,33]. This impact becomes particularly pronounced in shallow waters or during near-surface measurements, where the boundaries are much closer. To mitigate this, we incorporated a side lobe rejection setting of 90%. The utilization of Storm (v1.17.06) software provided by Nortek allowed for sophisticated filtration that not only facilitated data refinement by managing SNR and side lobe effects but also compensated for the tilting effect of the ADCP. Such comprehensive data processing ensures the robustness and reliability of the ADCP measurements.

Pulse correlation in ADCP measurements refers to the correlation between the transmitted and received acoustic signals. The accuracy of the velocity measurements made by an ADCP relies significantly on this pulse correlation. Acoustic pulses are transmitted into the water column and are reflected off suspended particles in the water. The reflected signal, which contains information about the motion of these particles, is then received back at the ADCP. If the received signal closely matches the transmitted signal, it signifies

a high pulse correlation. High correlation typically indicates that the signal has not been significantly distorted or altered during its transmission and reflection, leading to more accurate velocity data [34].

Low pulse correlation in ADCP data may occur due to various factors such as signal scattering, interference, or distortion, leading to a received signal that differs significantly from the transmitted one. Low correlation can affect the quality of the data, making it less reliable for accurately representing water velocities [35]. For instance, in cases of strong currents, the acoustic signal can be significantly altered during its round trip, resulting in lower pulse correlations and potential velocity ambiguities [36]. This issue can be more prominent in environments that are turbulent or contain bubbles, as these can distort the transmitted signal and decrease the correlation. In our study, the data was initially processed using Storm software, after which data with a pulse correlation lower than 50% were discarded [28].

2.4. Reynolds Stresses

Wind stress, the force exerted by wind on the water's surface, is intrinsically connected to momentum flux. Momentum flux can incite movement and mixing within the water column, rendering it a critical parameter in the investigation of turbulence and momentum transport in fluid systems. The term $\langle u'w' \rangle$ signifies the vertical Reynolds stress or turbulent momentum flux, which is a representative measure of momentum transfers due to turbulent fluctuations [37]. In this context, u', w', and $\langle \rangle$ symbolize the horizontal velocity fluctuation, vertical velocity fluctuation, and time-averaging, respectively.

Although momentum flux does not directly induce a mass flux, it may indirectly influence vertical mass flux by generating turbulence and initiating mixing processes arising from wind action on the surface [38]. Wind-induced turbulence originating from the surface amplifies vertical mixing in the water column, leading to a homogenization of water properties across different depths. When wind-induced shear stress is applied to a still water surface in contact with the atmosphere, an initially sharp exponential velocity profile begins to develop from the water's surface. A mean velocity profile displaying higher velocity at larger vertical positions generally exhibits a negative momentum flux [39]. As wind-induced turbulence heightens, this sharp profile slowly transitions into a blunt profile, promoting a downward mass movement.

The vertical momentum flux, quantifying the rate of momentum transfer vertically due to turbulence, critically determines the water column's motion and mixing. When the momentum flux is negative, it suggests a momentum transfer from the surface towards lower layers of the water column, indicative of amplified turbulence and vertical mixing within those strata. Therefore, interpreting vertical momentum fluxes is pivotal to comprehending the physical processes within the ocean's surface layer. We computed the Reynolds stresses to examine the wind's impact on the vertical momentum flux.

2.5. Stokes Drift

We evaluate the relative influence of Stokes drift on the dominant surface current due to its significant role in the dispersion of pollutants such as microplastics and oil slicks [40]. The most accurate portrayal of Stokes drift can be derived from a 2D wave spectrum [41]; however, obtaining this spectrum can sometimes be challenging. We used the monochromatic wave as a representation to elucidate the effects of Stokes drift. Horizontal particle velocity (*u*) for a deep-water Airy wave is provided as

$$u(z,t) = a\sigma e^{kz}\cos(kx - \sigma t) \tag{1}$$

where *a*, *k*, and σ are wave amplitude (= H/2), wave number (= 2π/L), and angular frequency (= 2π/T), respectively [42]. A fluid particle returns to its original position, forming a closed loop in a linear wave. but the second-order nonlinear effects are incorporated into the Taylor expansion of the particle velocity and subsequently time-averaged, the

time-mean vertical velocity profile of the Stokes wave for deep water waves [43] can be expressed as

$$u_s(z) = a^2 \sigma k e^{2kz} \tag{2}$$

To compute the Stokes drift profile from Equation (2), we utilized the significant wave height observed from a nearby buoy, the peak wave period from the wave spectrum acquired from LANSOP, and the wave length determined through the dispersion relation [44].

3. Results

3.1. Data Filtration

Exp1 was conducted under weak wind conditions, and with the ADCP range located below sea level, it was shielded from interference, leading to only a small fraction of data being filtered out. Conversely, Exp2 was conducted under moderate wind conditions, and the ADCP range intersected the sea level, leading to significant data removal. Upon applying the SNR thresholding and side lobe rejection filter, 0.03% (Exp1) and 23.63% (Exp2) of raw data were excluded via the Storm software. Figure 3 illustrates the distributions of raw data (depicted by the dashed line) and filtered data (depicted by the red lines). Following the removal of data with a low pulse correlation, 49% (Exp1) and 13% (Exp2) of the raw data remained, which were utilized for further analysis. The distribution of the remaining data is represented by the blue lines in Figure 3.
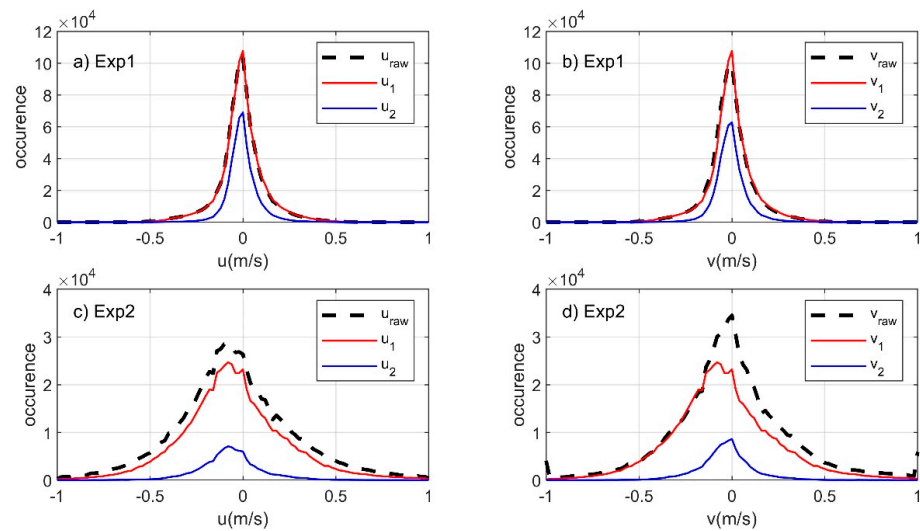

Figure 3. Distribution of horizontal current speed based on data filtration for Exp1 (**a**,**b**) and for Exp2 (**c**,**d**). The dashed line represents raw data. The red line illustrates the data remaining after the application of Signal-to-Noise (SNR) thresholding and side lobe rejection filters. The blue line indicates the residual data after applying the 50% pulse correlation criteria.

Figure 4 illustrates the temporal variations in the vertical profile of horizontal current speed following data filtration. Figures 4a and 4c, respectively, showcase the remaining current data for Exp1 and Exp2, after the application of SNR thresholding, side lobe rejection, and tilt compensation via the Storm software. The black lines represent sea surface level fluctuations as detected by pressure and tilt sensors installed on the ADCP. All data above these lines were discarded. Moreover, in the case of Exp2, a significant amount of data just beneath the sea surface level was also removed. Figure 4b,d depict the final remaining current data for Exp1 and Exp2, respectively, after the elimination of data with correlation values less than 50%.
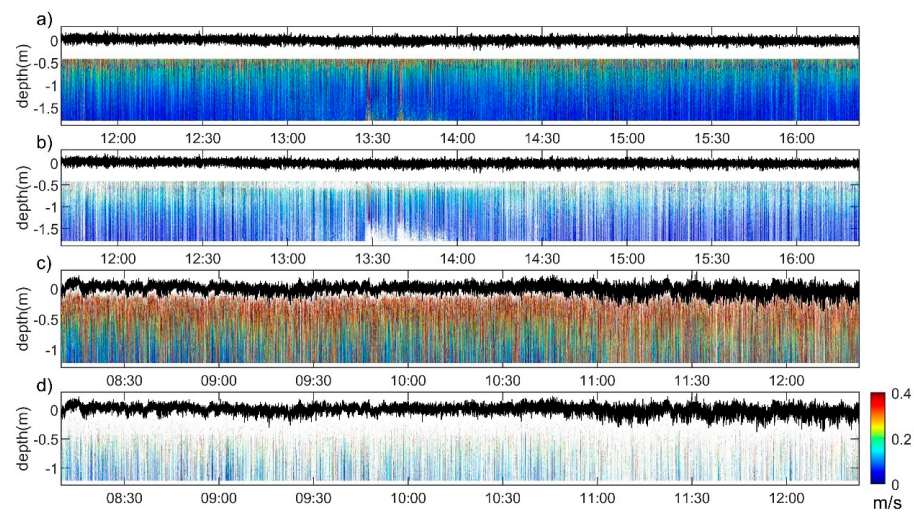
Figure 4. Data Filtration. Panels (**a**,**c**) illustrate the remaining horizontal current data following the application of Signal-to-Noise thresholding and side lobe rejection filters. Panels (**b**,**d**) display the remaining horizontal current data after the implementation of pulse correlation criteria filtering.

3.2. Hydrometeorological Observations

The experiments, Exp1 and Exp2, were conducted under weak (0–4 m/s) and mild wind (4–8 m/s) conditions, respectively. The hydrometeorological conditions including wind, wave, and surface current are presented in Figure 5. During Exp1 in May, the average wind speed and direction were 1.69 m/s and 202° (northward), respectively, with the wind persistently blowing northward throughout the experiment, exhibiting a standard deviation of 7.33° throughout the experiment. The mean significant wave height and wave direction were 0.49 m and 188° (northward), respectively, and the waves continued to propagate northward during the experiments with a standard deviation of 10.3°. Therefore, the wind and wave directions were almost identical. During Exp2 in November, the average wind speed and direction were 5.04 m/s and 262° (eastward), respectively. The wind continued to blow eastward, with a standard deviation of 12° throughout the experiment. The mean significant wave height was 0.46 m, and it increased towards the end of the experiment. As Exp2 was conducted within a bay area, the wave heights under mild wind conditions during Exp2 were comparable to those under weak wind conditions during Exp1. Based on wind speed observations and the drag coefficient parameterized by $C_d = (0.8 + 0.065U_{10})10^{-3}$ [45], the average wind stresses for Exp1 and Exp2 were estimated to be 0.0081 Pa and 0.035 Pa, respectively.

Time-series measurements of ADCP revealed a strong dependence of wave-induced near-surface current speed on depth and wind speed. To investigate the effect of waves, the magnitude of horizontal current speed U was calculated as $\sqrt{u^2 + v^2}$, where u and v are instantaneous ADCP current. As anticipated, an intensification of wave-induced horizontal current speed was observed within a 1 m depth, with stronger winds during Exp2 leading to stronger current speeds. Despite the overall calm weather conditions during Exp1, a wind event at around 1 pm notably enhanced vertical shear within 1 m depth. For both experiments, active shear variations were limited to the upper 1 m depth, where surface wave activity predominantly influences surface current.

Based on the near-surface current measurements at depths between -1.2 m and -0.4 m from both experiments, the horizontal surface current and vertical shear exhibited positive correlations with wind speed (Figure 6a,b). To minimize the influence of oscillatory surface waves on the current component, a 10 min moving average was implemented, so the horizontal current speed U was calculated as $\sqrt{(u)^2 + (v)^2}$, where u and v are 10 min moving averages of the ADCP current speed. The averaged horizontal current speed and vertical shear were 0.08 m/s and 0.32 m/s, respectively, for Exp1, and 0.15 m/s and

0.47 m/s for Exp2. Overall, the linear slopes fitted to all data were 0.013 for the horizontal current speed and 0.032 for the shear (Figure 6a,b).
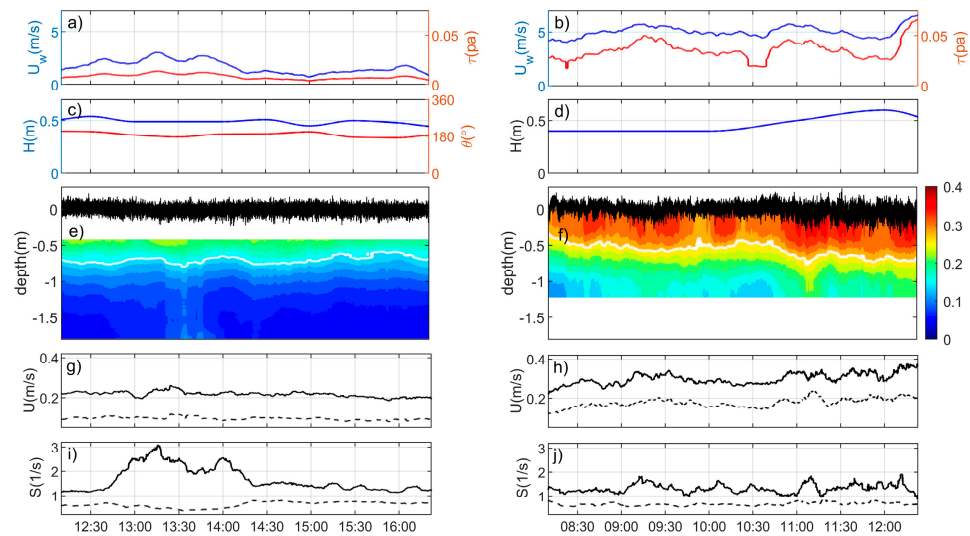

Figure 5. Hydrometeorological conditions and corresponding current measurements for Exp1 (left panels) and Exp2 (right panels). Time series of wind speed (U_w) and wind stress (τ) (**a,b**), wave height (H) and wave direction (θ) (**c,d**), vertical profiles of ADCP horizontal current speed (**e,f**), ACDP horizontal current speed at 0.5 m (solid lines) and 1.0 m (dashed lines) depths (**g,h**), and vertical shear (**i,j**). No wave direction information for Exp2 because it was conducted in the bay. White lines in (**e,f**) indicate the isolines of 0.15 m/s and 0.28 m/s, respectively. The horizontal current speed U was calculated as $\sqrt{u^2 + v^2}$. The instantaneous filtered current speeds were interpolated using neighboring points to generate the u and v components in this figure.
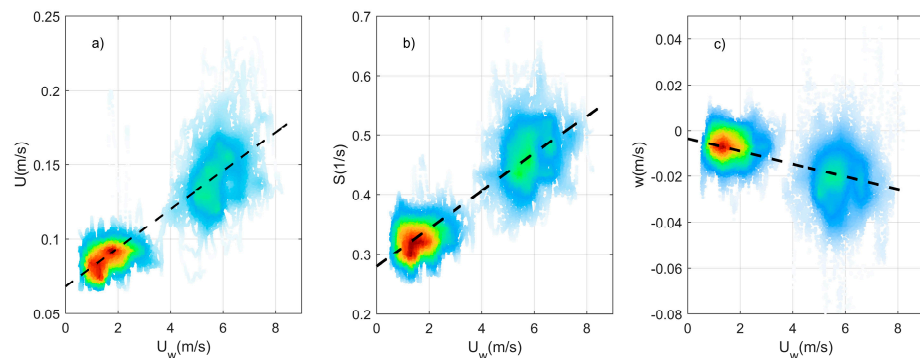

Figure 6. Scatter plots displaying the correlation between wind speed U_w and depth-averaged horizontal velocity U (**a**), depth-averaged shear S (**b**), and depth-averaged vertical velocity w (**c**). The density of data points is indicated by the color scale. Only data with a correlation greater than 50% were used in the analysis. Data were averaged over depths ranging from -1.2 m to -0.4 m for both experiments, and a 10 min moving average was subsequently applied. The horizontal velocity was calculated as $\sqrt{(u)^2 + (v)^2}$, where u and v are the 10 min moving averages of the ADCP current used to eliminate the effect of wave action. The vertical velocity was also subjected to a 10 min averaging. The dashed linear fitting lines are y = 0.013x + 0.068, y = 0.032x + 0.28, and y = -0.0028x + 0.0036 for (**a**), (**b**), and (**c**), respectively.

4. Discussions

4.1. Wind-Dependent Surface Current and Shear

Negative mean vertical velocities and their negative correlation with wind were observed in both experiments. The mean vertical velocity for Exp1 was near zero (-0.0071 m/s), whereas it was noticeably lower for Exp2, at -0.021 m/s. This difference manifested as a

negative slope of −0.0023 in the linear fit depicted in Figure 6c. A possible explanation for this negative mass flux could be the downwelling induced by buoyancy effects caused by density differences. For Exp1, the mean water temperatures measured by the Conductivity, Temperature, and Depth (CTD) sensor within the 0–2 m depths range, and the mean air temperature recorded by a nearby weather station were 14.7 °C and 20.62 °C, respectively. The positive temperature gradient (dT = 20.62−14.7 = 5.92 °C) at the air–sea interface resulted in a slightly positive temperature gradient in the 2 m depth water layer (dT = 0.025 °C). In contrast, for Exp2, the water and air temperatures were 17.65 °C and 10.96 °C, respectively, leading to a negative temperature gradient (dT = 10.96−17.65 = −6.69 °C), which in turn resulted in a slightly negative temperature gradient in the 2 m depth layer (dT = −0.021 °C). Additionally, for Exp2, the surface salinity as measured by the CTD was 0.06 psu higher than that at a 2 m depth, while no such difference was detected in Exp1. As such, the pronounced local negative vertical velocity observed in Exp2 may account for the buoyancy-induced transportation, suggesting that the temperature and salinity differences between the surface and subsurface waters could drive vertical mass transport in the water column [46,47].

4.2. Reynolds Stresses

We observed a vertical momentum flux that was negative in the wind direction and positive orthogonal to the wind direction. The correlation between horizontal and vertical velocities in the upper surface layer at depths ranging from −0.8 m to −0.4 m is depicted in Figure 7. Throughout Exp1, with a mean wind speed of 1.93 m/s, the wind consistently blew toward the North. The vertical momentum flux aligned with the wind direction ($\langle v'w' \rangle$) was negative, while the vertical momentum flux ($\langle u'w' \rangle$) aligned with the East direction, perpendicular to the wind, was positive. Similarly, throughout Exp2, with a mean wind speed of 5.04 m/s, the wind consistently blew toward the East. The vertical momentum flux aligned with the wind direction ($\langle u'w' \rangle$) was negative, whereas the vertical momentum flux ($\langle v'w' \rangle$) aligned with the North direction, perpendicular to the wind, was positive.
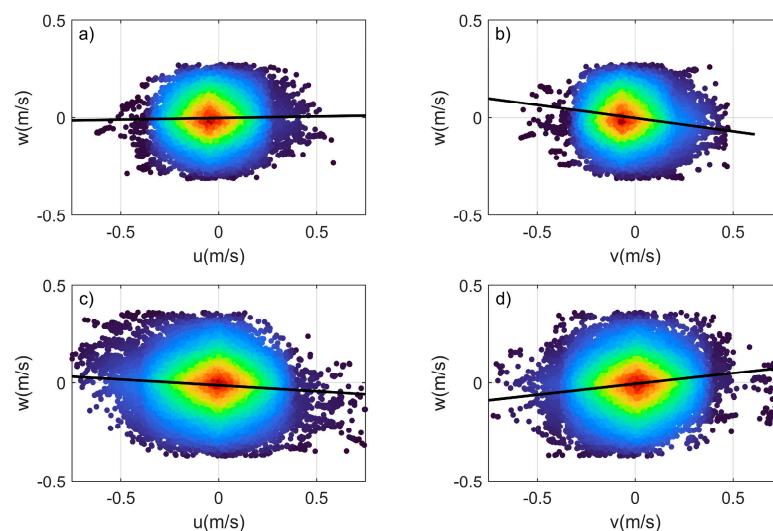

Figure 7. The correlation between horizontal velocity and vertical velocity is depicted. Panels (**a**,**b**) illustrate linear regression fittings for u vs. w and v vs. w for Exp1, respectively, while panels (**c**,**d**) depict linear regression fittings for u vs. w and v vs. w for Exp2, respectively. The slopes derived from these linear fittings are 0.017 (**a**), −0.14 (**b**), −0.060 (**c**), and 0.11 (**d**).

Negative momentum flux suggests that the momentum transfer is directed downwards, often a result of wind-induced shear stress at the water surface. When the momentum flux is negative, it can induce an evolution of the vertical velocity profile near the water surface. Initially, under calm conditions, the water is still, and the velocity profile is flat with essentially no vertical motion. However, when wind-induced shear stress begins

to act on the water surface, an exponential velocity profile starts to form, which is sharply peaked at the surface and decreases rapidly with depth. This is the initial response to the wind's influence. As the wind continues to exert stress on the water's surface and the negative momentum flux persists, the velocity profile starts to change further. The initially sharp profile becomes blunter, which is indicative of increased mixing and the transfer of momentum from the surface to deeper layers of the water. The wind-induced turbulence that is associated with the negative momentum flux enhances this mixing and momentum transfer, causing the vertical velocity profile to transform and the water properties at different depths to homogenize.

4.3. Spectral Variations of Near-Surface Current

Figure 8 depicts spectrograms for sea surface height (η), vertical shear (S), horizontal current speed (U), and vertical current speed (w), corresponding to wind speed during the experiments. The sea surface height (η) was calculated using data from the pressure sensor and was adjusted using readings from the tilt sensor in the ADCP. Significant energy peaks for η near 0.1 Hz were detected in both experiments, which are typically associated with swells originating from distant locations. A broad energy distribution around 0.3 Hz (Exp1) and 0.4 Hz (Exp2) pointed to the dominant surface waves. Notably, under weak wind conditions (Exp1), the spectral distribution was broader than under mild wind conditions (Exp2). During Exp2, an energy surge was detected after 11 am, coinciding with increases in wind speed and wave height. The spectral pattern of η was reflected in the spectrum for w, suggesting that the vertical particle velocity, which is comparable in magnitude to horizontal velocity in deep-water surface waves, is directly linked to vertical undulation. Therefore, the spectral distribution of η could potentially serve as a surrogate for the spectral distribution of vertical velocities near the surface.
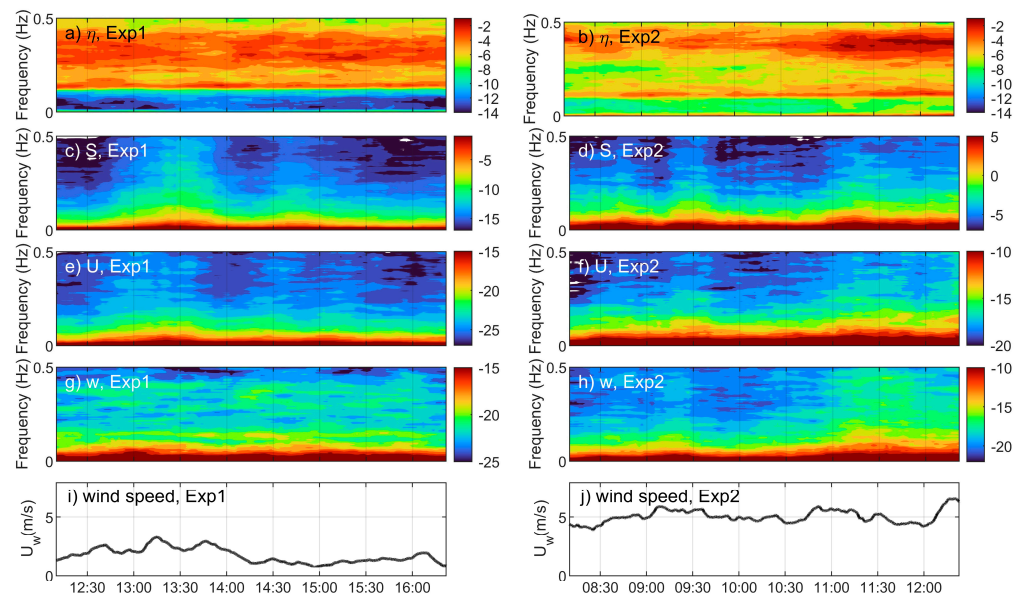

Figure 8. Spectrograms for different variables. Panels (**a**,**c**,**e**,**g**) represent the sea surface height (η), depth-averaged shear (S), depth-averaged horizontal current speed (U), and depth-averaged vertical speed (w), respectively, for Exp1. The same variables for Exp2 are displayed in panels (**b**,**d**,**f**,**h**). Panels (**i**,**j**) showcase the wind speed for Exp1 and Exp2, respectively. The horizontal current speed was subjected to a 2 min moving average, followed by depth-averaging across a range of -1.2 m to -0.4 m depths. The units of the contour plots are in decibels (dB).

Although variations in η were not strongly influenced by wind, the shear closely mirrored instantaneous wind fluctuations that were especially apparent during pronounced wind events at 13:00–14:00 (Exp1), 9:30 (Exp2), and 11:00 (Exp2). During periods of weaker

wind (Exp1), there was no significant enhancement of energy in the high-frequency domain. Conversely, stronger wind events, such as in Exp2, showed a broader energy distribution extending into the high-frequency spectral domain. Under weak wind conditions (Exp1), vertical velocity exhibited low sensitivity to wind variations, similar to the behavior of η.

4.4. Vertical Velocity Profiles and Stokes Drift

To investigate deeper into near-surface current shear, we juxtaposed the ADCP measurements in our experiments with data presented in Laxague et al. [19] (henceforth termed as LAX2017). Given that ADCP measurements are interpreted as current fluctuations and the speed of LANSOP as the average current velocity, the LANSOP mean speed was added to the ADCP profiles to construct the total the velocity profile. This profile aligned well with an exponential function as illustrated in Figure 9. The wind speed in Exp2, which was three times stronger than in Exp1, aligns with the surface current in Exp2 being approximately three times more potent. The velocity magnitudes in LAX2017 largely aligned with our findings. LAX2017's measurements in the deeper layer (depths less than 1 m) were akin to our Exp1 results, while their upper layer measurements (depths higher than 1 m) paralleled our Exp2 results in terms of magnitude.
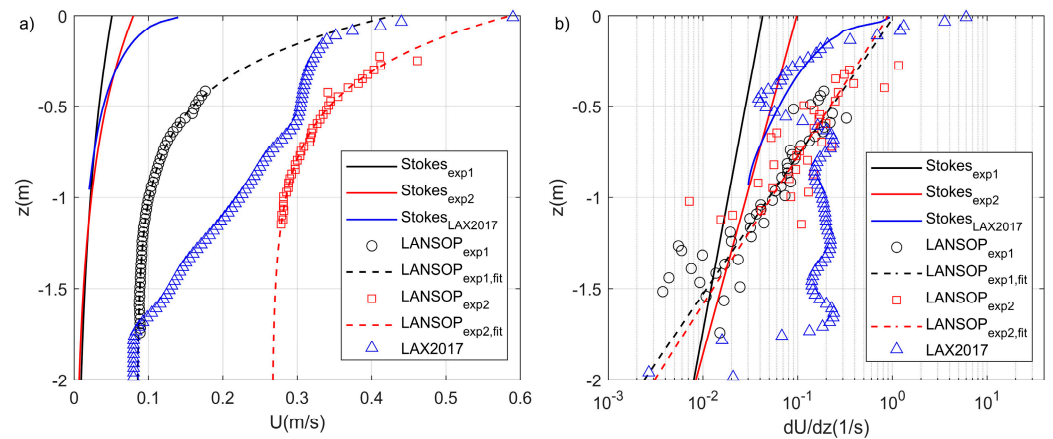

Figure 9. (**a**) Time-averaged vertical velocity profiles observed in Exp1 ('○'), Exp2 ('□'), and LAX2017 ('△'), alongside estimates of Stokes drift (solid lines). The dashed lines represent exponential fittings. LAX2017 references the integrated profile reported in Laxague et al. 2017, where Stokes drift was estimated for 0–1 m depths (blue color). (**b**) Vertical shear profiles derived from the vertical velocity profiles shown in (**a**). The same line colors, line types, and markers were used in both (**a**) and (**b**). Given the consistent northward wind during Exp1 and eastward wind during Exp2, only the v and u components were used for their respective experiments.

We computed the vertical velocity profiles of Stokes drift for deep water waves using Equation (2), as displayed in Figure 9a, and interpreted the wave-induced velocity profile based on the significant wave height and period of the dominant wave component. The Stokes drift in both Exp1 and Exp2 exhibited similarities despite the stronger wind observed in Exp2. This resemblance might be due to Exp2's location within a bay area. In the case of LAX2017, the Stokes drift component demonstrated a pronounced velocity within the top 20 cm of the surface layer.

The surface current shear measurement was an order of magnitude higher than the shear induced by Stokes drift on the surface. The measurements from the LANSOP revealed near-surface mean shear values between order of 0.1–1 m/s for depths <1 m, and order of 0.01–0.1 m/s for depths 2 m–1 m depths. Although the LANSOP measurements largely aligned with those from LAX2017, the shear cited in LAX2017 were notably an order of magnitude higher for depths below 1 m (Figure 9b).

4.5. Estimation of Microplastic Shear Dispersion

To estimate the contribution of Stokes drift to the total velocity and shear depicted in Figure 9, we computed the ratio (r_u) of Stokes drift current to the time-averaged total current (Figure 10a) and the ratio (r_S) of Stokes drift shear to the time-averaged total shear (Figure 10a). The total velocity (or mass transport) was estimated to be around 10 times larger than that of Stokes drift, and the total shear was about 5 times larger than that produced by Stokes drift in the TSL. The primary factor for the increased total mass transport and shear is believed to be direct wind-driven current [40], which is particularly responsive to local wind events, as demonstrated in the spectrograms in Figure 8.
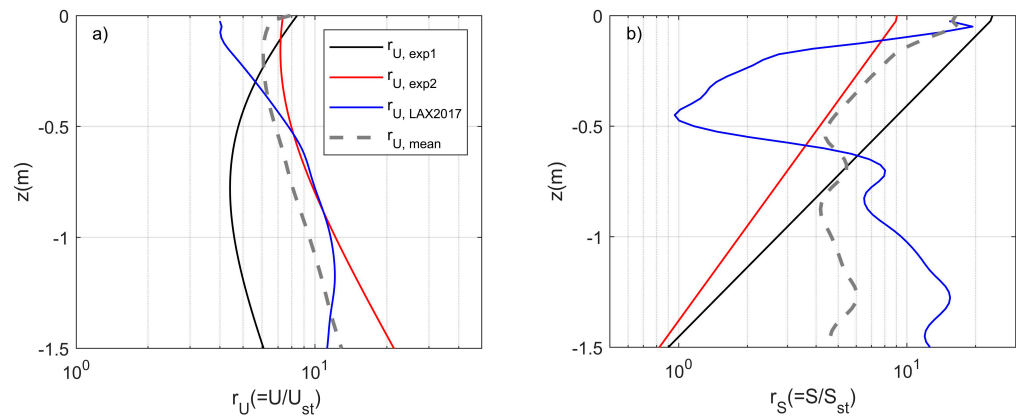

Figure 10. Assessment of the Stokes drift's contribution to the overall observed surface current. (**a**) Ratio (r_U) of the time-averaged total current to the estimated Stokes drift current for Exp1 (black line), Exp2 (red line), and LAX2017 (blue line). (**b**) Ratio (r_S) of the time-averaged total shear to the Stokes drift shear, using the same line representations. Stokes drifts for Ex1 and Ex2 were estimated by Equation (2). The gray dashed lines indicate the mean of three datasets (Exp1, Exp2, and LAX2017). Depth-averaged (0–1.5 m depths) $r_{U,exp1}$, $r_{U,exp2}$ $r_{U,LAX2017}$, and $r_{U,mean}$ are 5.8, 15.8, 9.4, and 10.3. Depth-averaged $r_{S,exp1}$, $r_{S,exp2}$ $r_{S,LAX2017}$, and $r_{S,mean}$ are 5.6, 2.8, 8.4, and 5.6.

The transport and dispersion of microplastics within the top surface layer (TSL) is a complex process influenced by both horizontal and vertical dynamics. Drawing from a simple dispersion model accounting for mean shear current (S) and vertical diffusivity (K_z) within a well-mixed bounded ocean layer, the horizontal dispersion coefficient K_x in the x-direction can be expressed as $K_x = S^2 h^4 / 60 K_z$ [30,48]. This relationship underscores two core interactions: while the shear squared demonstrates a direct correlation with the horizontal dispersion coefficient, vertical mixing displays an inverse relationship.

When we examine the behavior of buoyant microplastics, predominantly confined to the TSL, the disparity in shear effects becomes clear. As illustrated in Figure 10, the ratio (r_S) reveals that Stokes drift by itself contributes to 1/25 of the horizontal dispersion coefficient (K_x) with respect to shear. This implies that the shear in the TSL developed directly by local wind stress plays a dominant role in the horizontal dispersion of buoyant microplastics. However, it is important to note that the wind enhancing shear-induced dispersion also boosts vertical mixing, which may counteract the horizontal dispersion [49]. For a well-rounded understanding of optimal dispersion of microplastics, comprehensive measurements of mean vertical shear should be paired with a quantification of vertical mixing.

5. Conclusions

In this study, we developed a Lagrangian observational platform, specifically designed for measuring mean vertical current profiles in the top surface layer while passively drifting with ocean currents. Based on the near-surface measurements, the study underscored several pivotal observations and implications:

- Vertical momentum flux: we observed a negative flux, aligned with the wind direction.

- Negative mass flux: we detected indications of negative mass flux, potentially due to buoyancy-induced downwelling or wind-induced turbulence.
- Stokes drift contribution: Stokes drift represents about 1/10 of total mass transport and 1/5 of shear in the TSL.
- Shear dispersion of microplastic: local wind-driven current amplifies horizontal dispersion, whereas wind-induced vertical mixing can potentially counteract this horizontal dispersion of microplastics.
- Measurement and parameterization: for accurate microplastic modeling, an integrated approach is essential, fusing precise shear measurements with vertical mixing assessments and subsequent parameterization.
- Wind-driven current vs. Stokes drift: contrary to common parameterizations that emphasize Stokes drift, our result underscores the pivotal role of direct wind-driven current in the horizontal dispersion of microplastics.

Our study emphasizes the significance of the Lagrangian near-surface observational platform, which provides insights into air–sea interaction and near-surface dispersion of microplastic. To precisely model the physical behavior of buoyant microplastics, it is essential to incorporate parameterizations that consider both the Stokes drift and the direct, local wind-driven current, an element frequently neglected in many models. Future experiments are set to enhance measurement accuracy by using Acoustic Doppler Velocimeters (ADV) and ultrasonic anemometers, shedding light on vertical mixing and momentum fluxes arising from multiscale air–sea interactions.

Author Contributions: Conceptualization, J.M.C.; methodology, J.M.C.; Software, J.M.C.; validation, J.M.C.; investigation, J.M.C., formal analysis. J.-H.L., investigation, J.-H.L.; writing—original draft preparation, J.M.C.; writing—review and editing, J.-H.L.; visualization, J.M.C.; supervision, J.M.C.; project administration, J.-H.L.; funding acquisition, J.-H.L. All authors have read and agreed to the published version of the manuscript.

Institutional Review Board Statement: Not applicable.

Informed Consent Statement: Not applicable.

Data Availability Statement: Not applicable.

Conflicts of Interest: The authors declare no conflict of interest.

References

1. Fairall, C.W.; Bradley, E.F.; Rogers, D.P.; Edson, J.B.; Young, G.S. Bulk parameterization of air-sea fluxes for tropical ocean-global atmosphere coupled-ocean atmosphere response experiment. *J. Geophys. Res. Ocean.* **1996**, *101*, 3747–3764. [CrossRef]
2. Wanninkhof, R.; Asher, W.E.; Ho, D.T.; Sweeney, C.; McGillis, W.R. Advances in quantifying air-sea gas exchange and environmental forcing. *Annu. Rev. Mar. Sci.* **2009**, *1*, 213–244. [CrossRef] [PubMed]
3. Large, W.G.; Pond, S. Open ocean momentum flux measurements in moderate to strong winds. *J. Phys. Oceanogr.* **1981**, *11*, 324–336. [CrossRef]
4. Edson, J.B.; Jampana, V.; Weller, R.A.; Bigorre, S.P.; Plueddemann, A.J.; Fairall, C.W.; Miller, S.D.; Mahrt, L.; Vickers, D.; Hersbach, H. On the exchange of momentum over the open ocean. *J. Phys. Oceanogr.* **2013**, *43*, 1589–1610. [CrossRef]
5. Breivik, Ø.; Janssen, P.A.; Bidlot, J.R. Approximate Stokes drift profiles in deep water. *J. Phys. Oceanogr.* **2014**, *44*, 2433–2445. [CrossRef]
6. Jenkins, A.D. Wind and wave induced currents in a rotating sea with depth-varying eddy viscosity. *J. Phys. Oceanogr.* **1987**, *17*, 938–951. [CrossRef]
7. McWilliams, J.C.; Restrepo, J.M. The wave-driven ocean circulation. *J. Phys. Oceanogr.* **1999**, *29*, 2523–2540. [CrossRef]
8. Drennan, W.M.; Graber, H.C.; Hauser, D.; Quentin, C. On the wave age dependence of wind stress over pure wind seas. *J. Geophys. Res. Atmos.* **2003**, *108*, 8062. [CrossRef]
9. Reisser, J.; Shaw, J.; Hallegraeff, G.; Proietti, M.; Barnes, D.K.; Thums, M.; Wilcox, C.; Hardesty, B.D.; Pattiaratchi, C. Millimeter-sized marine plastics: A new pelagic habitat for microorganisms and invertebrates. *PLoS ONE* **2014**, *9*, e100289. [CrossRef]
10. Liubartseva, S.; Coppini, G.; Lecci, R.; Creti, S. Regional approach to modeling the transport of floating plastic debris in the Adriatic Sea. *Mar. Pollut. Bull.* **2016**, *103*, 115–127. [CrossRef]

11. Iwasaki, S.; Isobe, A.; Kako, S.I.; Uchida, K.; Tokai, T. Fate of microplastics and mesoplastics carried by surface currents and wind waves: A numerical model approach in the Sea of Japan. *Mar. Pollut. Bull.* **2017**, *121*, 85–96. [CrossRef] [PubMed]
12. Van Sebille, E.; Aliani, S.; Law, K.L.; Maximenko, N.; Alsina, J.M.; Bagaev, A.; Bergmann, M.; Chapron, B.; Chubarenko, I.; Cózar, A.; et al. The physical oceanography of the transport of floating marine debris. *Environ. Res. Lett.* **2020**, *15*, 023003. [CrossRef]
13. Zhang, H. Transport of microplastics in coastal seas. *Estuar. Coast. Shelf Sci.* **2017**, *199*, 74–86. [CrossRef]
14. Li, Y.; Zhang, H.; Tang, C. A review of possible pathways of marine microplastics transport in the ocean. *Anthr. Coasts* **2020**, *3*, 6–13. [CrossRef]
15. Isobe, A.; Kubo, K.; Tamura, Y.; Nakashima, E.; Fujii, N. Selective transport of microplastics and mesoplastics by drifting in coastal waters. *Mar. Pollut. Bull.* **2014**, *89*, 324–330. [CrossRef]
16. Chubarenko, I.; Bagaev, A.; Zobkov, M.; Esiukova, E. On some physical and dynamical properties of microplastic particles in marine environment. *Mar. Pollut. Bull.* **2016**, *108*, 105–112. [CrossRef]
17. Löder, M.G.; Gerdts, G. Methodology used for the detection and identification of microplastics—A critical appraisal. In *Marine Anthropogenic Litter*; Springer: Cham, Switzerland, 2015; pp. 201–227.
18. Kukulka, T.; Proskurowski, G.; Morét-Ferguson, S.; Meyer, D.W.; Law, K.L. The effect of wind mixing on the vertical distribution of buoyant plastic debris. *Geophys. Res. Lett.* **2012**, *39*, L07601. [CrossRef]
19. Laxague, N.J.; Özgökmen, T.M.; Haus, B.K.; Novelli, G.; Shcherbina, A.; Sutherland, P.; Guigand, C.M.; Lund, B.; Mehta, S.; Alday, M.; et al. Observations of near-surface current shear help describe oceanic oil and plastic transport. *Geophys. Res. Lett.* **2018**, *45*, 245–249. [CrossRef]
20. Richman, J.G.; De Szoeke, R.A.; Davis, R.E. Measurements of near-surface shear in the ocean. *J. Geophys. Res. Ocean.* **1987**, *92*, 2851–2858. [CrossRef]
21. Cronin, M.F.; Kessler, W.S. Near-surface shear flow in the tropical Pacific cold tongue front. *J. Phys. Oceanogr.* **2009**, *39*, 1200–1215. [CrossRef]
22. Wenegrat, J.O.; McPhaden, M.J.; Lien, R.C. Wind stress and near-surface shear in the equatorial Atlantic Ocean. *Geophys. Res. Lett.* **2014**, *41*, 1226–1231. [CrossRef]
23. Rusello, P.J. *A Practical Primer for Pulse Coherent Instruments*; Nortek Technical Note No.: TN-027; Nortek, Inc.: Carlsbad, CA, USA, 2009; Volume 117, 17p.
24. Davis, R.E. Drifter observations of coastal surface currents during CODE: The method and descriptive view. *J. Geophys. Res. Ocean.* **1985**, *90*, 4741–4755. [CrossRef]
25. Lumpkin, R.; Özgökmen, T.; Centurioni, L. Advances in the application of surface drifters. *Annu. Rev. Mar. Sci.* **2017**, *9*, 59–81. [CrossRef]
26. Mullarney, J.C.; Henderson, S.M. Lagrangian measurements of turbulent dissipation over a shallow tidal flat from pulse coherent Acoustic Doppler Profilers. *Coast. Eng. Proc.* **2012**, *33*, 1–12. [CrossRef]
27. Déjeans, B.S.; Mullarney, J.C.; MacDonald, I.T. Lagrangian observations and modeling of turbulence along a tidally influenced river. *Water Resour. Res.* **2022**, *58*, e2020WR027894. [CrossRef]
28. Thomson, J. Wave breaking dissipation observed with "SWIFT" drifters. *J. Atmos. Ocean. Technol.* **2012**, *29*, 1866–1882. [CrossRef]
29. Taylor, G.I. Diffusion by continuous movements. *Proc. Lond. Math. Soc.* **1922**, *2*, 196–212. [CrossRef]
30. Choi, J.M.; Troy, C.D.; Hawley, N. Shear dispersion from near-inertial internal P oincaré waves in large lakes. *Limnol. Oceanogr.* **2015**, *60*, 2222–2235. [CrossRef]
31. Deines, K.L. Backscatter estimation using broadband acoustic Doppler current profilers. In Proceedings of the IEEE Sixth Working Conference on Current Measurement, San Diego, CA, USA, 11–13 March 1999; Cat. No. 99CH36331. IEEE: New York, NY, USA, 1999; pp. 249–253.
32. Onwuka, I.S.; Scinto, L.J.; Fugate, D.C. High-Resolution Estimation of Suspended Solids and Particulate Phosphorus Using Acoustic Devices in a Hydrologically Managed Canal in South Florida, USA. *Sensors* **2023**, *23*, 2281. [CrossRef]
33. Lentz, S.J.; Kirincich, A.; Plueddemann, A.J. A note on the depth of sidelobe contamination in acoustic Doppler current profiles. *J. Atmos. Ocean. Technol.* **2022**, *39*, 31–35.
34. Stacey, M.T.; Monismith, S.G.; Burau, J.R. Measurements of Reynolds stress profiles in unstratified tidal flow. *J. Geophys. Res. Ocean.* **1999**, *104*, 10933–10949. [CrossRef]
35. Gordon, R.L. *Acoustic Doppler Current Profiler-Principles of Operation: A Practical Primer*; RD Instruments, Inc.: La Gaude, France, 1996; 54p.
36. Lohrmann, A.; Hackett, B.; Røed, L.P. High resolution measurements of turbulence, velocity and stress using a pulse-to-pulse coherent sonar. *J. Atmos. Ocean. Technol.* **1990**, *7*, 19–37. [CrossRef]
37. Tennekes, H.; Lumley, J.L. *A First Course in Turbulence*; MIT Press: Cambridge, MA, USA, 1972.
38. Moum, J.N.; Perlin, A.; Klymak, J.M.; Levine, M.D.; Boyd, T.; Kosro, P.M. Convectively driven mixing in the bottom boundary layer. *J. Phys. Oceanogr.* **2004**, *34*, 2189–2202. [CrossRef]
39. Kundu, P.K.; Cohen, I.M.; Dowling, D.R. *Fluid Mechanics*; Academic Press: Cambridge, MA, USA, 2015.
40. Onink, V.; Wichmann, D.; Delandmeter, P.; van Sebille, E. The role of Ekman currents, geostrophy, and stokes drift in the accumulation of floating microplastic. *J. Geophys. Res. Ocean.* **2019**, *124*, 1474–1490. [CrossRef]
41. Breivik, Ø.; Bidlot, J.R.; Janssen, P.A. A Stokes drift approximation based on the Phillips spectrum. *Ocean Model.* **2016**, *100*, 49–56. [CrossRef]

42. Dean, R.G.; Dalrymple, R.A. *Water Wave Mechanics for Engineers and Scientists*; World Scientific Publishing Company: Singapore, 1991; Volume 2.
43. Salmon, R. Introduction to Ocean Waves. Scripps Institution of Oceanography, University of California: San Diego, CA, USA, 2008.
44. Hunt, J.N. Direct solution of wave dispersion equation. *J. Waterw. Port Coast. Ocean. Div.* **1979**, *105*, 457–459. [CrossRef]
45. Wu, J. Wind-stress coefficients over sea surface near neutral conditions—A revisit. *J. Phys. Oceanogr.* **1980**, *10*, 727–740. [CrossRef]
46. Gregg, M.C.; D'Asaro, E.A.; Riley, J.J.; Kunze, E. Mixing efficiency in the ocean. *Annu. Rev. Mar. Sci.* **2018**, *10*, 443–473. [CrossRef] [PubMed]
47. Klymak, J.M.; Moum, J.N.; Nash, J.D.; Kunze, E.; Girton, J.B.; Carter, G.S.; Lee, C.M.; Sanford, T.B.; Gregg, M.C. An estimate of tidal energy lost to turbulence at the Hawaiian Ridge. *J. Phys. Oceanogr.* **2006**, *36*, 1148–1164. [CrossRef]
48. Okubo, A. The effect of shear in an oscillatory current on horizontal diffusion from an instantaneous source. *Int. J. Oceanol. Limnol* **1967**, *1*, 194–204.
49. Sundermeyer, M.A.; Price, J.F. Lateral mixing and the North Atlantic Tracer Release Experiment: Observations and numerical simulations of Lagrangian particles and a passive tracer. *J. Geophys. Res. Ocean.* **1998**, *103*, 21481–21497. [CrossRef]